Matter-wave analog of a fiber-optic gyroscope

Katarzyna A. Krzyzanowska,[1] Jorge Ferreras,[1,2] Changhyun Ryu,[1] Edward Carlo Samson,[1,3] and Malcolm G. Boshier[1]
[1]*Materials Physics and Applications Division, Los Alamos National Laboratory, Los Alamos, New Mexico 87545, USA*
[2]*Rutherford Appleton Laboratory, Didcot OX11 0QX, United Kingdom*
[3]*Department of Physics, Miami University, Oxford, Ohio 45056, USA*

(Received 27 July 2023; accepted 23 August 2023; published 10 October 2023)

Confining the propagating wave packets of an atom interferometer inside a waveguide can substantially reduce the size of the device while preserving high sensitivity. We have realized a two-dimensional Sagnac atom interferometer in which Bose-condensed ^{87}Rb atoms propagate within a tight waveguide formed by a collimated laser beam, a matter wave analog of the fiber optic gyro. The condensate is split, reflected, and recombined with a series of Bragg pulses while the waveguide moves transversely so that the wave-packet trajectories enclose an area. Delta-kick cooling is used to prepare low-density atomic wave packets with a temperature of 3 nK. The low density reduces the impact of interatomic interactions, while the low temperature limits the expansion of the wave packet during the interferometer cycle. The effective enclosed area is 0.8 mm^2 with an average fringe contrast of 20% and underlying contrast up to 60%. The main source of the reduced average contrast is phase noise caused by mechanical vibrations of the optical components. We present a measurement of Allan deviation for such an atom rotation sensor, showing that the interferometer phase noise falls with averaging time τ as $\tau^{-1/2}$ for τ up to 10 000 seconds. The statistical noise falls below the Earth rotation rate after 30 minutes of averaging.

DOI: 10.1103/PhysRevA.108.043305

I. INTRODUCTION

Atom interferometers [1,2] have important applications in fundamental science [3,4] and as accelerometers, gravimeters, and rotation sensors [4,5]. The last rely on the Sagnac effect: rotation at rate $\mathbf{\Omega}$ of an atom interferometer whose arms enclose area A creates a phase shift $\varphi_{Sg} = \frac{2m}{\hbar}\mathbf{\Omega}\cdot\mathbf{A}$, where m is the atomic mass [6]. While free-space atom interferometers have demonstrated the high sensitivity of this technique [7], their size must grow quadratically with interrogation time to accommodate free-fall under gravity. This ultimate limitation has motivated numerous efforts to confine propagating matter waves in tight waveguides [8–15], analogous to light in the fiber optic gyro (FOG) [16], to deliver long interrogation times and large enclosed total area, and hence large sensitivity, in a small physics package. These factors are especially important for inertial navigation and other applications that require a compact transportable rotation sensor.

An atom interferometer gyro's performance limit is determined by its rotation sensitivity (proportional to the Sagnac area A) and by the quantum projection noise set by the particle flux and measurement rate [17]. The Angular Random Walk (ARW) of a shot noise-limited atom interferometer is $\theta_{ARW} = \hbar/2mA\sqrt{N}\sqrt{\nu}$, where N is the number of atoms and ν is the measurement rate. With a circular trajectory for atoms moving with velocity v and a repetition rate limited by an interrogation time T, this expression becomes $\theta_{ARW} = \hbar\pi/(2mv^2T^{3/2}\sqrt{N})$. Typically, atom interferometers can achieve a signal-to-noise ratio (SNR) of the order of 10^2, corresponding to the shot noise limit for $N = 10^4$ atoms [18,19]. Improving the SNR further will require better atom detection techniques and precise noise control, which are immensely difficult for the current state of the art. For $N = 10^4$ atoms, a shot noise-limited ^{87}Rb atom interferometer would need an interrogation time of $T = 1.5$ s to achieve the ARW of $10^{-4}\,^\circ\sqrt{\text{h}}$ demonstrated by the best FOGs [20,21]. Much longer interrogation times of several seconds are of course desirable to deliver even better performance. While achieving such interrogation times for thermal atoms is challenging because of the unavoidable wave-packet dispersion, the narrow momentum width of BECs allows for extended interaction times and enables Bragg diffraction into a single momentum order [22–24]. Therefore, a tight guide and BEC wave packets are essential components of a practical matter wave analog of a FOG.

The first approach towards this goal of realizing the matter wave analog of a FOG used cold thermal atoms in guiding potentials formed by weak (few Hz) magnetic traps [25,26]. In [25] short Bragg pulses created a thin phase grating which diffracted atoms into multiple momentum orders. The resulting trajectories formed closed loops when the guide was translated during the interferometer cycle, resulting in an atomic density grating pattern which could be probed by Bragg scattering. The pairing of BEC and Bragg diffraction was used in [27] to realize an atom interferometer enclosing 0.1 mm^2 by imparting transverse motion to the moving wave packets through a sudden displacement of the relatively weak (6 Hz) harmonic trap. Other approaches to creating trapped Sagnac atom interferometers where the splitting is based on manipulations of the potential have demonstrated much smaller enclosed area [28] and [12]. Recently, a novel architecture where BEC wave packets are displaced to opposite sides of a weak harmonic potential and subsequently launched into circular trajectories has been shown to achieve 0.5 mm^2 enclosed area [29].

In this paper we report a tightly guided BEC Sagnac atom interferometer. The tight waveguide confinement perpendicular to the wave-packet velocity makes it analogous to the FOG and will make the device much less sensitive to platform motion than the weakly trapped approaches discussed above. The interferometer wave packets are trapped by the optical dipole potential of a collimated laser beam, enabling use of an $m_F = 0$ state which is first-order insensitive to magnetic fields and hence to magnetic field gradients. Also, with the optical waveguide, phase fluctuations due to guiding potential fluctuations are mostly common mode. These characteristics make the optically guided interferometer much more robust against environment magnetic field noise than its magnetically guided counterpart. Our design also has a straightforward extension to multiaxis measurement without requiring that the sensor be rotated or that gravity be compensated. In addition to reporting the biggest Sagnac area reported to date, 0.8 mm^2, we also present an Allan deviation measurement for a guided Sagnac atom interferometer along with an in-depth study of the noise behavior of the device.

II. EXPERIMENTAL SETUP

The BEC hardware is a modified version of the setup described in [12]. A $^{8}7$Rb BEC in the first-order magnetically insensitive state $|F = 1, m_F = 0\rangle$ and containing between 500 and 1500 atoms is prepared in a tight crossed-dipole trap formed at the intersection of a horizontal 1064 nm laser beam with waist 13 μm and a vertical 1064 nm beam with waist 60 μm and transverse trapping frequency $2\pi \times 140$ Hz. The 60 s cycle time of the experiment is dominated by the evaporative cooling stage in this trap. The interferometer waveguide is formed by a horizontal collimated 1064 nm laser beam [Fig. 1(a)] propagating collinear with the tight horizontal beam. The BEC is transferred adiabatically from the tight beam to the waveguide beam, still confined axially by the vertical beam. The waveguide power and waist are, respectively, 550 mW and 60 μm, giving axial and radial trapping frequencies of $2\pi \times 0.3$ Hz and $2\pi \times 200$ Hz. The waveguide beam can be translated horizontally over a few mm by the acousto-optic deflector (AOD) and lens shown in Fig. 1(a). It passes through the cell at a 12° angle of incidence to avoid undesirable interference resulting from multiple reflections at the cell windows.

Next, the confining vertical beam is switched off to allow the condensate to expand along the waveguide for 20 ms. The wave-packet expansion which is undesirable during the interferometer cycle is then frozen with a 1.5 ms pulse of the vertical beam which realizes a δ-kick cooling potential [30]. The resulting wave packet has an axial temperature of 3 nK and an axial size of ≈70 μm FWHM (see Appendix A). The interferometer cycle starts immediately after the δ-kick pulse. The interferometer beamsplitters and mirrors are realized with pulses of a 780 nm standing wave formed by retro-reflection of a beam with 5.42 mm waist overlapped with the waveguide using two dichroic mirrors, as shown in Fig. 1(a).

As shown in Fig. 1(b), the BEC initially in momentum state $|p = 0\rangle$ is split into a superposition of two wave packets with momentum $p = \pm 2\hbar k$, where $k = 2\pi/\lambda$ using a double square pulse of the Bragg laser [22,23,25,27].

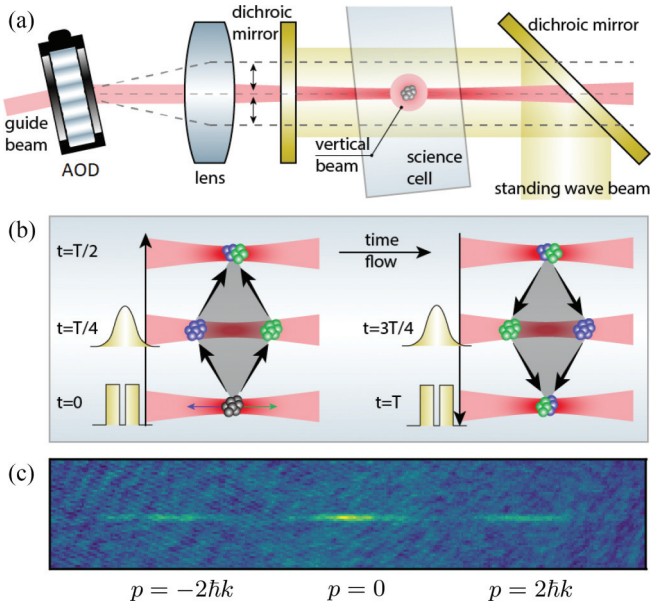

FIG. 1. (a) Experimental setup; (b) interferometer sequence. Blue and green colors of atoms correspond to the $+2\hbar k$ and $-2\hbar k$ momentum components, respectively. The time flow follows the black arrows. (c) Experimental data acquired $\Delta t = 12$ ms after the recombination pulse, with atoms in two channels: $|p = 0\rangle$ and $|p = \pm 2\hbar k\rangle$.

The two wave packets propagate in opposite directions with speed $v = 11.7\,\text{mms}^{-1}$ while the waveguide is transversely moved out and back to the starting position [25]. To create an interferometer with total interrogation time T, Gaussian reflection pulses [31] are applied at times $T/4$ and $3T/4$, followed by a second double square pulse which serves as a recombination pulse. During this process the atoms follow the diamond-shape trajectory shown in Fig. 1(b), enclosing a Sagnac area proportional to both vT and the transverse displacement of the waveguide. The waveguide is translated with a time-dependent acceleration that minimizes the transverse excitation of the atoms at the final position [32]. In our system this allows for transport of atoms up to 2 mm in 40 ms.

The two output ports of the interferometer are the momentum states $p = 0$ and $p = \pm 2\hbar k$. The BEC evolves in the guide for 10 ms after the recombination pulse, allowing the momentum components to separate into three wave packets easily detected via absorption imaging [in Fig. 1(c)]. For an interferometer with zero Sagnac phase, the population of atoms in each port $\{N_{p=0}, N_{\pm 2\hbar k}\}$ depends on the interferometer phase ϕ as

$$P(\phi) = \frac{N_{p=0}}{N_{\text{total}}} = \frac{1}{2}[a\cos(\phi + \phi_0) + C], \tag{1}$$

where N_{total} is the total atom number in the three ports, and a, C, and $\phi 0$ are, respectively, the amplitude, offset, and phase shift of the fringe. The interferometer phase ϕ is

$$\phi = 2(\phi_1 - 2\phi_2 + 2\phi_3 - \phi_4), \tag{2}$$

where ϕ_i is the phase of the ith Bragg pulse [Fig. 1(b)]. The interferometer phase ϕ can be experimentally adjusted by changing the frequency f of the Bragg laser by Δf right

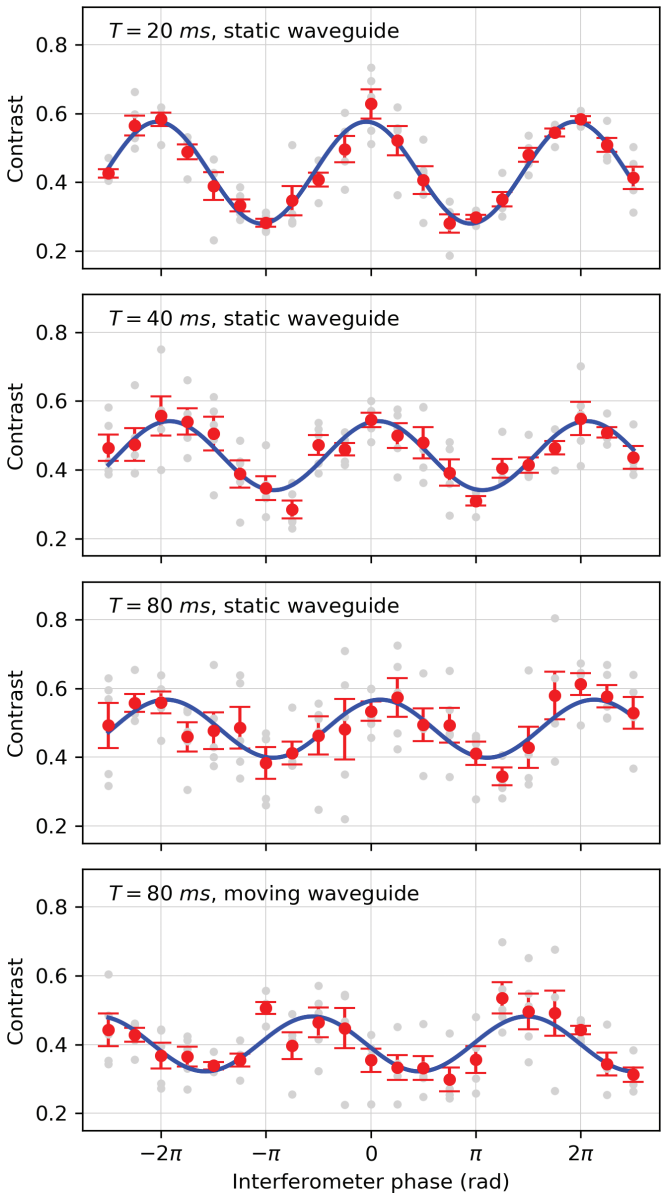

FIG. 2. Interferometer fringes for a static waveguide atom interferometer with interrogation times $T = 20$, 40, and 80 ms and for a moving waveguide interferometer with $T = 80$ ms. Gray points represent the raw data for a single experimental run. Each red data point is an average of five repetitions for the given interferometer phase. Error bars are the standard error in those mean values.

before the recombination pulse, which changes the interferometer phase by

$$\Delta\phi = 8\pi L \Delta f / c, \tag{3}$$

where $L = 12.3$ cm is the distance from atoms to the retroreflector. This approach can scan ϕ over at least 4π, as shown in Fig. 2.

III. RESULTS

The interferometer has been operated in two modes: a static waveguide interferometer enclosing zero Sagnac area and the rotation-sensitive configuration obtained with the moving waveguide. The static mode aids optimization and characterization by decoupling any effects caused by waveguide movement from fundamental limitations of the system. Figure 2 shows interference fringes recorded for interrogation times $T = 20$ ms, 40 ms, and 80 ms in the static mode, along with one moving guide fringe with $T = 80$ ms. The full $\pm\frac{5}{2}\pi$ interferometer scan was obtained by tuning the frequency of the final pulse over ± 0.75 GHz. Five measurements of $P(\phi)$ data at each phase are averaged and fitted to the function in Eq. (1). In this data set, the moving guide encloses 0.8 mm^2, which is the largest Sagnac area enclosed by a fully guided atom interferometer reported to date.

Figure 2 shows that there is a phase shift $\Delta\phi \approx 0.5\pi$ rad between the moving and static guide interferometers for 80 ms interrogation times. Since both experiments were conducted under the same conditions this phase shift is presumably caused by the waveguide movement. Possible mechanisms include misalignment of the Bragg beam with the guide beam or center of mass motion excited by intensity fluctuations if the waveguide is tilted. While both mechanisms will be investigated and minimized in future work, the phase shift should not impact rotation sensing performance because the rotation rate can be obtained through a differential measurement with multiple Sagnac areas [7].

The behavior of both the underlying and average fringe contrast with interrogation time evident in Fig. 2 can provide useful information about imperfections and noise processes in the interferometer. Factors impacting the underlying contrast have been extensively studied in [33], which showed that a residual axial curvature of the approximately collimated guide imparts a spatially varying phase shift to the wave packets that can lead to decreased fringe visibility. The analysis showed that this effect can be minimized by ensuring the interferometer is symmetrical, wave-packet size remains constant, and the timing of the Bragg pulses is optimized. The δ-kick cooling technique employed in our interferometer helps in this regard because it minimizes wave-packet size changes during the interferometer cycle. Residual axial curvature also decreases the time at which the wave packets overlap during the recombination pulse by an amount $\delta T \approx 2\omega_a^2 (T/4)^3$ in a waveguide with axial frequency ω_a [33]. For our interferometer with $\omega_a = 2\pi \times 0.3$ Hz and total interrogation time $T = 80$ ms the timing shift is $\delta T \approx 0.06$ ms, which is negligible here. In future experiments with longer interrogation times the effect will become important, requiring that the Bragg pulse timing be adjusted accordingly.

A. Noise analysis

Since a detailed study of the fringe contrast supported by an appropriate noise model might reveal factors limiting the system, static mode fringes for our standard set of $T = 20$ ms, 40 ms, and 80 ms with many repetitions per interferometer phase were collected over several hours to produce a large data set for further analysis (Fig. 3). The raw data presented in Fig. 3 right column (red points) show that the range of $P(\phi)$ values is roughly the same for all three interrogation times, while the fluctuations of $P(\phi)$ at each phase increase with interrogation time. There are two intrinsic noise sources for all atom interferometers: shot noise and phase diffusion [28]. Shot noise is negligible compared to the noise visible seen

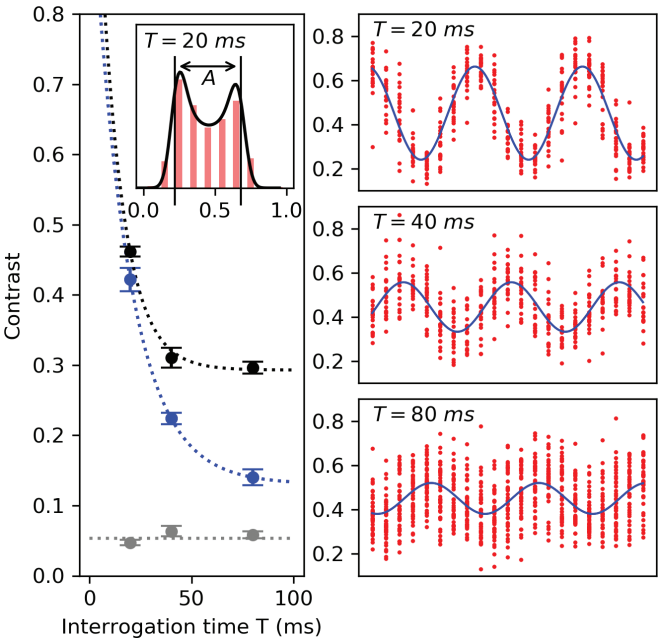

FIG. 3. Interferometer fringe contrast as a function of interrogation time T. (Right) Each interferometer scan was repeated 22 times for $T = 20$ ms and 40 ms, and 43 times for $T = 80$ ms. The blue sine curves are unweighted fits of Eq. (1) to the data. (Left) The blue data points show the amplitude of the sinusoidal fits as a function of interrogation time T. The underlying contrast (black points) and the offset noise (gray points) were obtained by fitting the noise model discussed in the text to each phase of the fringe. The dotted curves are to guide the eye. The inset plot shows a histogram of all data points in the $T = 20$ ms fringe. The distance A is the underlying contrast of the fringe.

in the fringes presented here. An estimate of the reduction in average contrast due to phase diffusion [34–44] says that the average contrast will still be 90% of the maximum value at $T = 80$ ms (see Appendix C). So it appears that the current interferometer is limited by technical noise.

Factors that could cause fluctuations in $P(\phi)$ [Eq. (1)] include noise in the interferometer phase ϕ, noise in the underlying contrast a, and noise in the offset C. A known source of technical noise in our experiment is mechanical vibrations of the Bragg retro-reflector mirror that cause changes in the phase of the Bragg pulses at the location of the atoms: If the optical table supporting the experiment is not floated the resulting phase noise causes all measurements to average to the same value within the error bars for all phases ϕ, even for our shortest interferometer time $T = 20$ ms.

The shape of a histogram of the $P(\phi)$ values recorded for multiple scans over the fringe (inset in Fig. 3 left column) provides information about sources of noise in $P(\phi)$. Pure phase noise does not change the shape of the histogram from the harmonic distribution of a noiseless interferometer. So the blurred edges of the histogram in Fig. 3 suggest that there is at least one other source of technical noise. The noise model has three free parameters: underlying contrast A, phase noise σ_ϕ, and offset noise σ_c. With sufficiently good statistics it becomes possible to determine the dependence of those three contributions on interrogation time T (see Appendix B).

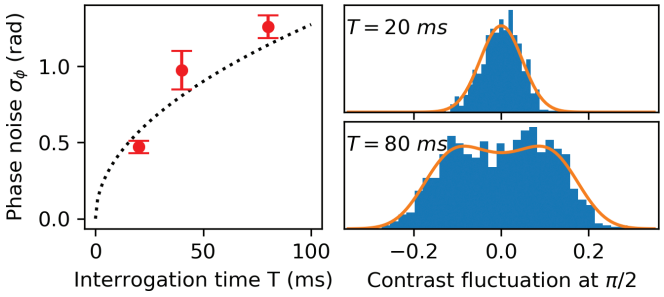

FIG. 4. Noise dependence on the interrogation time T. (Left) Standard deviation of the phase noise σ_ϕ of the contrast values distribution P_i at the steep side of the fringe $\phi = \pi/2$. The fit is $c\sqrt{T}$. (Right) The histogram of the atoms fraction distribution minus the average value of the full set $P_i - \bar{P}$. The noise model with standard deviation σ_ϕ determines the shape of the orange curves. Both histograms consist of about 800 samples total.

The decreasing amplitude $a(T)$ of the fitted fringes (blue curves) versus the interrogation time is shown in the left part of Fig. 3 as blue points. The decreasing trend is a result of averaging over all possible sources of noise. The underlying amplitude A in the fitted noise model (black points) also decreases with interrogation time. At this stage we can only speculate on what causes the decrease in the underlying contrast, but it is possible that the experiment was just not as well optimized for $T = 40$ ms and $T = 80$ ms as it was for $T = 20$ ms.

The noise model analysis of the fringes shows that the offset noise is constant (gray points in Fig. 3 left), while the phase noise increases significantly with interrogation time. The phase noise σ_ϕ obtained from the noise model is plotted against the interrogation time in Fig. 4 (left) and appears to scale $\propto \sqrt{T}$. Figure 4 (right) shows the distribution of the measured atom population $P(\phi)$ at the steepest point of the fringe ($\phi = \pi/2$). The distribution for $T = 20$ ms is Gaussian whereas the distribution for $T = 80$ ms has two visible peaks away from the mean value. This is consistent with the noise analysis and indicates that the Gaussian phase fluctuation grows with time and exceeded $\pi/4$ at $T = 80$ ms. The conclusion obtained from this analysis is that, since the offset noise remains constant, the dominant source of noise for interferometer interrogation times longer that 20 ms is mechanical vibrations of the retro-reflection mirror.

While the unknown source of offset noise makes removing it difficult without further in-depth studies, the phase noise can be removed using the technique presented in [45]. Here the performance of an atom interferometer operated in the especially harsh environment of an aircraft in flight was greatly improved by mounting a high-performance accelerometer on the retro-reflector and thereby correcting for vibration-induced changes in its position during the interferometer cycle. In addition, engineering better mounting solutions for the retro-reflector will also improve interferometer performance.

B. Long-term stability

The capacity to average measurements for a long time is key for precision measurement. Accordingly, the long-term

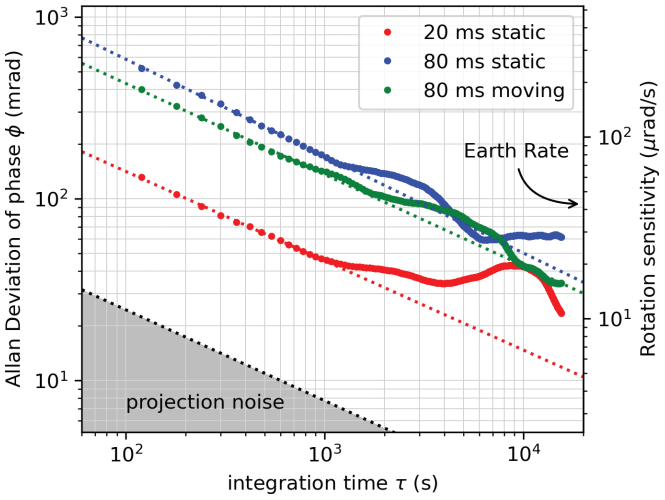

FIG. 5. Overlapping Allan deviation scaled by the corresponding underlying contrast for different interferometer cycle times. The projection noise is computed as $1/a\sqrt{N}$ for $a = 1$ and $N = 1000$. The right-hand axis shows the corresponding rotation sensitivity of the $T = 80$ ms moving guide interferometer which has 0.8 mm^2 enclosed area. The arrow labeled Earth Rate corresponds to a projection of the Earth's rotation vector onto the horizontal loop area in New Mexico.

stability of our system has been assessed by measuring the Allan deviation [46] of the interferometer phase at the steepest point of the fringe over 12 hours for three cases: static 20 ms interferometer, static 80 ms interferometer, and moving 80 ms interferometer. Results are presented in Fig. 5 for integration times τ up to 5.5 hours. The 60 s cycle time of the experiment determines the minimum integration time $\tau = 120$ s. The plot shows that the Allan deviation scales $\propto 1/\sqrt{\tau}$ for all three cases. The extrapolated values at $\tau = 1$ s are 1300 mrad and 2600 mrad for $T = 20$ ms and $T = 80$ ms respectively. The Allan deviations for stationary and moving 80 ms interferometer are in good agreement, indicating that moving the waveguide does not influence the stability of the device even though a phase shift is induced by translating the waveguide. The Allan deviation measurement shows that the sensitivity after 2000 s ($\approx$30 min) of averaging is comparable to the Earth's rotation rate (42 μrads^{-1} in New Mexico) for the $T = 80$ ms moving waveguide Sagnac interferometer.

IV. DISCUSSION AND CONCLUSIONS

In summary, we have demonstrated a BEC matter wave analog of a fiber optic gyro. It encloses the largest Sagnac area (0.8 mm^2) achieved for a waveguide device. The total interrogation time was extended up to 80 ms by implementing a form of δ-kick cooling to reduce the BEC temperature, generating dilute wave packets that remain collimated throughout the interferometer cycle and suppressing phase diffusion. The average fringe contrast decreases with interrogation time, primarily due to phase fluctuations produced by mechanical vibrations of the retro-reflector forming the standing wave for the Bragg pulse beamsplitters and mirrors. Statistical analysis shows that the dominant noise source is Gaussian (white power spectrum), with the Allan deviation falling with averaging time τ as $\tau^{-1/2}$ for τ up to 10 000 seconds.

The architecture of our guided Sagnac atom interferometer offers some advantages over other approaches. In addition to increasing the Sagnac area, the use of two reflections instead of one creates a symmetry which suppresses contrast loss due to residual axial curvature [33] and makes the device insensitive to constant acceleration along the guide. The interferometer is relatively insensitive to changes in the waveguide laser intensity; while the guide beam power was stabilized to $\approx$1% before the AOM, the guide beam power in the cell varied systematically by about 20% with guide movement due to the AOM's frequency response. It is known that the mode of the beam might be distorted by an AOM. While not important here, these issues will be addressed in future work with increased Sagnac area by stabilizing the guide power after the science cell, and by replacing the AOM with a piezo-controlled mirror.

In most guided AI designs, measuring rotation along a horizontal axis entails turning the device on its side, which will require some form of gravity compensation to nullify the effects of gravity on the now vertical wave-packet trajectories. An advantage of our approach is that replacing our current 1D AOD with a 2D AOD and a folding mirror will enable waveguide translation along all three axes and hence three-axis measurement with a single fixed-orientation device without gravity compensation. Although it is possible to engineer a device performing measurements along all axes simultaneously, by, for instance, combining three independent sensors, the most straightforward implementation with the current setup is to perform measurement along each axis sequentially. This will decrease the bandwidth of our sensor by a factor of 3, but it will not affect the performance of the device otherwise. Moreover, the tight transverse confinement in our FOG analog ($\approx$200 Hz) will provide good protection against platform motion. In comparison, multiaxis measurement may be more challenging in architectures based on wave packets orbiting in weak ($\approx$2 Hz) bowl-like potentials, where both platform motion and tilting the potential would result in asymmetric trajectories that degrade performance [29]. Moreover, the bandwidth of our interferometer, where a single measurement is a direct measurement of Sagnac phase, should be higher than that of differential devices [29] where phase determination requires reconstruction of a relative phase ellipsoid comprising several interferometer cycles. The statistical sensitivity demonstrated in this work will make possible a precise measurement of the rotation rate of the Earth within 30 minutes using a differential scheme with multiple Sagnac areas.

It should be possible to improve the performance of our device by several orders of magnitude [19]. Future work will focus on increasing the Sagnac area to increase the sensitivity to rotation. The current experimental limitations on area are the trap depth of the moving guide and the AOD deflection range, which together limit the maximum distance over which atoms can be translated within the coherence time. It will be possible to increase both the waveguide trap depth and the distance over which the guide is moved by changing the hardware. Also, since the interferometer phase noise is dominated by vibrations of the retro-reflecting mirror forming

the standing wave, adding a suitable accelerometer to the retro-reflector [45] and engineering that part of the system to improve its stability will increase the coherence time. That will in turn allow us to demonstrate multiple round-trips in the waveguide loop [47], which is a major advantage of the waveguide geometry. We will also increase the wave-packet momentum using optimized Bragg pulse shapes [48], which will further increase the area enclosed in a given interrogation time. For example, with wave-packet momentum $10\hbar k$, implementation of 200 round trips as demonstrated in [47], and higher laser power of 100 W allowing for roughly 10 times further guide translation due to increased radial trap frequency, the expected enclosed area will be $80\,\mathrm{cm}^2$. The combination of this increased area with the noise level of the current device would lead to an angular random walk (ARW) of $0.0004\,^\circ/\sqrt{\mathrm{h}}$, which is similar to that of state of the art FOGs [21,49].

ACKNOWLEDGMENTS

We thank D. Anderson for helpful discussions of his previous work on waveguide Sagnac atom interferometers. This work was funded by DARPA under the A-PhI program. The initial development of the experimental apparatus was supported by the Office of Naval Research and by the Laboratory Directed Research and Development program of Los Alamos National Laboratory under Project No. 20180045DR.

APPENDIX A: DELTA-KICK COOLING

Delta-kick cooling (DKC) [30] applies a pulsed harmonic confining potential to a condensate to manipulate its momentum distribution. In this work DKC is applied after the BEC is prepared in a crossed-dipole trap formed of two perpendicular 1064 nm beams having waist $\omega_0 = 60\,\mu\mathrm{m}$: a horizontal guide beam and a vertical beam. Here the vertical beam provides tight confinement of the BEC along the guide beam axis.

After the vertical beam is switched off, the condensate expands freely along the waveguide for 20 ms before the vertical beam is pulsed on for 1.6 ms to provide the DKC confining potential. The size of the cloud along the guide σ_a is obtained by fitting absorption images with 2D Gaussian function:

$$g(x,y) = \exp\left[-\frac{(x-x_0)^2}{2\sigma_a^2} - \frac{(y-y_0)^2}{2\sigma_r^2}\right], \qquad \text{(A1)}$$

where σ_r is size in the radial direction of the guide, and (x_0, y_0) is the position of the center of the cloud.

The cloud expansion with and without DKC as a function of expansion time t is illustrated in Fig. 6. The data are fitted with a simple thermal expansion model

$$\sigma(t) = \sqrt{\sigma_{t=0}^2 + \frac{k_B T_{BEC}}{m_{Rb}} t(t-2t_f)} \qquad \text{(A2)}$$

to obtain the temperature T_{BEC} of the condensate, where m_{Rb} is the rubidium mass, k_B is Boltzmann's constant, $\sigma_{t=0}$ is the size of the cloud at $t = 0$, and t_f the time at which focusing of the BEC occurs. When no δ-kick cooling is applied, the cloud expands rapidly with temperature $\approx$25 nK. With DKC the cloud is weakly focused at $t_f = 38$ ms after the DKC pulse. The much slower subsequent expansion with DKC corresponds to a temperature of 3 nK.

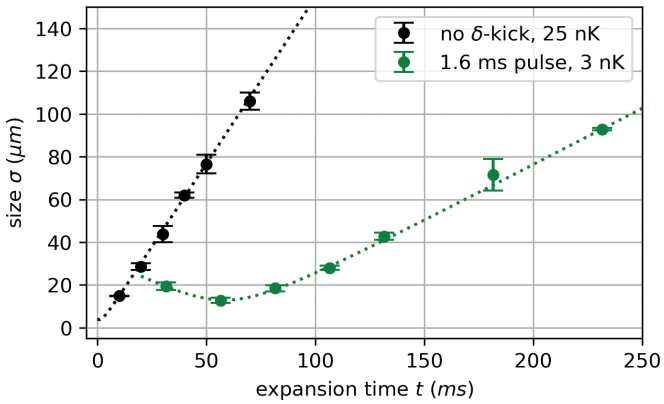

FIG. 6. BEC size σ_a along the guide for variable expansion time t. Each data point is a mean of three measurements with an error bar given by the standard error in the mean. The dotted lines are a fit of Eq. (A2) to the data, finding temperatures of 25(3) nK without δ-kick cooling, and 2.95(8) nK with a 1.6 ms δ-kick pulse.

The final temperature delivered by our DKC implementation is currently limited by technical factors. We find that a pulse duration of 1.6 ms results in the lowest temperature and the most symmetric size evolution over a 80 ms interferometer interrogation time. Increasing the duration of the DKC pulse beyond this does not decrease the temperature further, because the expansion dynamics are predominantly governed by the mean-field energy of the condensate. The expansion time before the DKC pulse is limited by the size of the vertical beam. The size of the cloud after initial expansion of 20 ms reaches $\mathrm{FWHM}_{BEC} \approx 70\,\mu\mathrm{m}$, which is comparable to the size of the beam. Increasing both the power and the size of the vertical beam should lead to even lower temperatures.

APPENDIX B: NOISE MODEL

Here we present a noise model describing the histogram of $P(\phi)$, the $p = 0$ fraction in the interferometer output ports. It extends the model containing only normally distributed offset noise used in [45] to extract information about readout noise. Our model contains two normally distributed variables: interferometer phase ϕ with standard deviation σ_ϕ and an additive offset noise with standard deviation σ_c. Even though this case study is applied to interferometer data, the model also holds for any type of data described by sinusoidal behavior.

Let us first recall that the fraction of atoms in the $p = 0$ interferometer output port is

$$P(\phi) = \frac{N_{p=0}}{N_{\mathrm{total}}} = \frac{1}{2}\left[a\sin\left(\phi - \frac{\pi}{2}\right) + C\right], \qquad \text{(B1)}$$

where a is the amplitude of the fringe.

In the first step we will derive the model for phase noise only, assuming $C = 0$ and neglecting $\pi/2$ term for simplicity. This means that the distribution is centered around 0. If a probability density function (PDF) of the phase ϕ is known, then one can use it to derive a PDF of the atom fraction P. Following this argument, the total probability of the measured data reflects the probability of the noisy variable

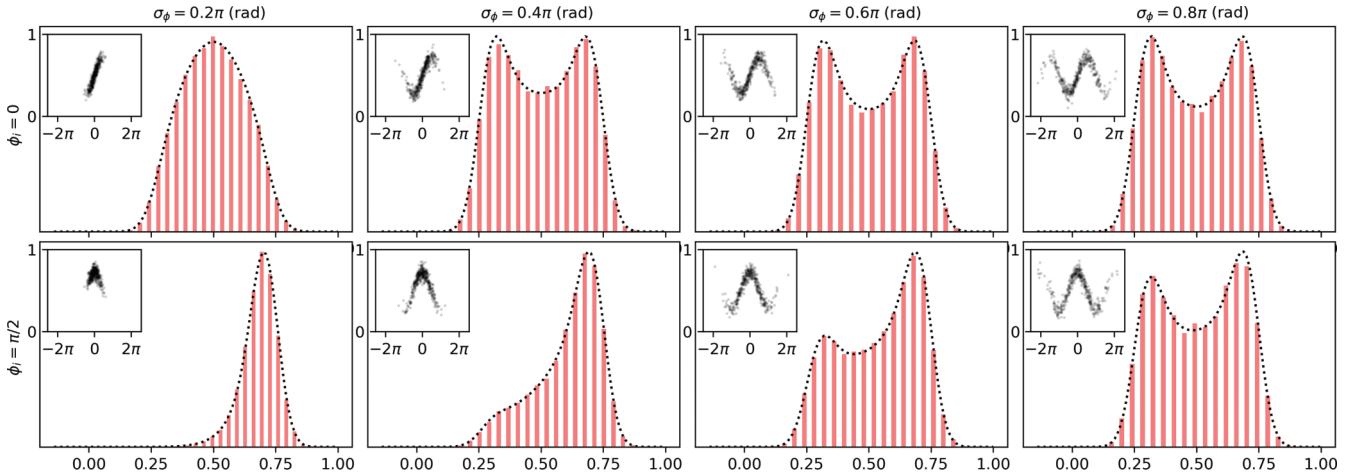

FIG. 7. Influence of phase and offset noise on the output of the interferometer. Synthetic data were obtained by adding normally distributed phase and offset noise to the interferometer fringe function Eq. (B1) for fixed values of $\phi_i = 0$ and $\phi_i = \frac{\pi}{2}$. The offset noise $\sigma_c = 5\%$ remains the same for all the graphs, while the phase noise increases from left to right. Inserts show how the phase fluctuation explores the fringe. The black dotted line is the noise model calculated for given values of ϕ_i, σ_ϕ and σ_c using Eq. (B5).

$f_P(P)dP = f_\varphi(\phi)d\phi$. Since the contributions from the normal distribution of phase ϕ can exceed $\pi/2$, the formula for $f_\varphi(\phi)$ takes the form

$$f_\varphi(\phi) = \frac{1}{\sqrt{2\pi}\sigma_\phi} \sum_{n=-\infty}^{\infty} \exp \frac{[\phi - (-1)^n \phi_i - n\pi]^2}{-2\sigma_\phi^2}, \quad \text{(B2)}$$

where ϕ is limited to $\langle -\pi/2, \pi/2 \rangle$ and ϕ_i is the Bragg phase. Changing variables from ϕ to P [using $\frac{d\phi}{dP}$ and $\phi(P) = \arcsin(2P/a)$] and combining it with the expression for $f_\varphi(\phi)$, one finds

$$f_P(P) = 2f_\varphi[\phi(P)]/a\sqrt{1 - (2P/a)^2}. \quad \text{(B3)}$$

Since the histogram of the data represents the probability that certain outcome is within a finite range of values, the equation above needs to be integrated to represent the quantity measured in the experiment accurately, giving

$$F(P) = \frac{1}{2} \sum_{n=-\infty}^{\infty} \operatorname{erf}\left[\frac{\arcsin \frac{2P}{a} - (-1)^n \phi_i - n\pi}{\sqrt{2}\sigma_\phi} \right]. \quad \text{(B4)}$$

Equation (B4) evaluated for bins of the histogram $F(P)|_{P_i}^{P_{i+1}}$ is an accurate representation of the histogram data. In the following step the additive independent normal noise σ_c can be introduced by calculating the convolution of the $F(P)$ and Gaussian distribution:

$$[F(P) * g(P)] = \left[F(P) * \frac{1}{\sqrt{2\pi}\sigma_c} \exp\left\{ -\frac{P^2}{2\sigma_c^2} \right\} \right]. \quad \text{(B5)}$$

The convolution is easily calculated numerically, allowing the model to be implemented to analyze the data in this paper. Figure 7 shows how the histogram shape for measurements depends on the noise. The important feature of the model is that phase and offset noise are orthogonal. Moreover, even for a substantial phase noise close to $\sigma_\phi < \pi$, where values of the phase explore more than one fringe, the model can be used to determine the exact value of phase noise spread σ_ϕ.

If the experimental data are obtained by repeating the measurement for a series of discrete interferometer phases $[\phi_1, \phi_1, \ldots, \phi_n]$, then the histogram of the full data set is simply a sum of Eq. (B5) over the entire set,

$$\sum_{\phi_i} [F(P, \phi_i) * g(P)]. \quad \text{(B6)}$$

Figure 8 (right column) shows a comparison between the model and a synthetic data set obtained by adding normally distributed noise to a cosine curve described by Eq. (B1). As shown by the figure, the model (dotted black line) is in a good agreement with the synthetic data (histogram bars). The comparison clearly shows that the histogram has sharp edges for an interferometer where the phase fluctuation is a dominant source, while the edges are blurred when the contribution to noise from other sources is significant.

Even though the noise model presented here does not include noise in the amplitude, it can still help distinguish between phase noise, which is a typical source of noise in interferometers, and other sources of technical noise.

APPENDIX C: PHASE DIFFUSION

Phase diffusion is known to be one of the intrinsic factors limiting the performance of atom interferometers. It has been observed and studied in various architectures [34–44]. The diffusion rate for an approach where atoms are split and recombined nonadiabatically using Bragg pulses, similarly to the setup used in our experiment, was theoretically studied in [41]. Here the effect of phase diffusion is considered to be created only by the fluctuations of the atom numbers in each cloud, which are governed by a binomial distribution.

Following the discussion in [41,44], the effect of the interatomic interactions in a many-body Hamiltonian is captured by the interaction coefficient g,

$$g = \frac{U_0}{2} \int |\psi_\pm|^4 \, \mathbf{dr}, \quad \text{(C1)}$$

where $U_0 = 4\pi\hbar^2 a_{sc}/M$, with M the atomic mass, a_{sc} the s-wave scattering length, and $\psi_\pm$ wave functions of two separate clouds after splitting. Here the wave function $\psi_\pm$ of each

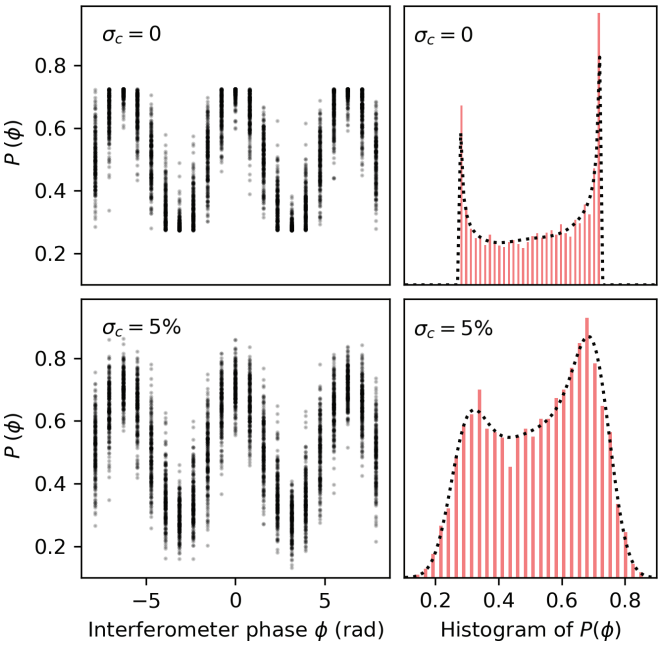

FIG. 8. Simulated interferometer data and the corresponding histograms of $P(\phi)$, the relative atom population in the $p = 0$ port. Blue curves show the interferometer fringe with no noise. The individual data points were obtained using Eq. (B1), with fixed amplitude $a = 0.45$ and normally distributed phase noise around $\phi_0 = 0$ [rad] with standard deviation $\sigma_\phi = 0.4$ [rad]. The upper row shows the fringe and the histogram for no offset noise $\sigma_c = 0$, while the offset noise $\sigma_c = 0.05$ [rad] is introduced in the bottom row. The dotted lines represent the noise model for each histogram obtained from Eq. (B6).

cloud is normalized to 1. The accumulated nonlinear phase ξ per atom is then obtained by integration of the interaction coefficient g over interrogation time T:

$$\xi = \frac{1}{\hbar}\int_0^T dt g. \tag{C2}$$

Knowing the accumulated phase ξ and the total number of atoms N, the averaged fringe visibility V is described by

$$V = \exp\{-2\xi^2 N\}. \tag{C3}$$

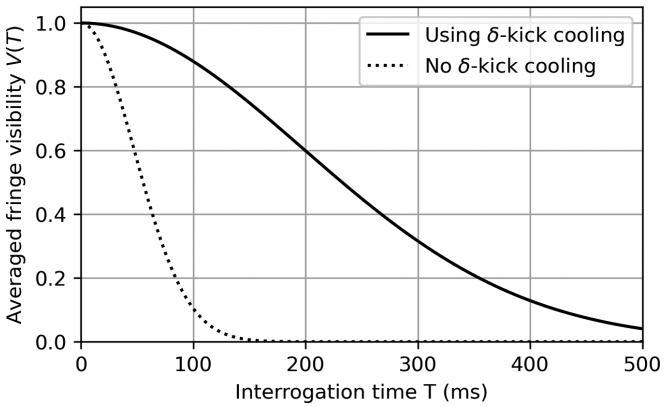

FIG. 9. Effect of phase diffusion on the fringe visibility as a function of the total interrogation time T, for $N = 1000$ atoms. The solid curve shows fringe visibility for an expanded δ-kicked cooled atomic cloud, while the dashed line is calculated for the cloud before the expansion. Both calculations are based on Eq. (C4) and assume constant size of the cloud during the interrogation time.

We calculated the accumulated phase ξ from the density profile of the cloud $|\psi_\pm|^2 = n(\mathbf{r})$, which was measured experimentally. Since, in our case, the wave-packet size does not change significantly during the interrogation time due to the δ-kick cooling technique, we can assume constant size of the split clouds. The formula used to obtain fringe visibility $V(T)$ versus interrogation time T in Fig. 9 takes the following form:

$$\xi(T) = \frac{U_0}{2\hbar} T \int n(\mathbf{r})^2 \, \mathbf{dr}. \tag{C4}$$

Figure 9 shows two cases: fringe visibility for an expanded (δ-kick cooled) cloud with FWHM $\approx$50 μm, and for a cloud before the expansion with FWHM $\approx$15 μm. In the first case, the phase diffusion effect is not significant for the interrogation times up to $T = 80$ ms used in the experiment. However, fringe visibility for the denser cloud present before expansion decreases significantly faster. Even though the calculation for the small cloud is less accurate because the assumption of constant size is not valid, it is still a useful reference point, indicating that the δ-kick cooling technique is essential for obtaining high-contrast interferometer fringes.

[1] O. Carnal and J. Mlynek, Young's double-slit experiment with atoms: A simple atom interferometer, Phys. Rev. Lett. **66**, 2689 (1991).

[2] D. W. Keith, C. R. Ekstrom, Q. A. Turchette, and D. E. Pritchard, An interferometer for atoms, Phys. Rev. Lett. **66**, 2693 (1991).

[3] K. Bongs, M. Holynski, J. Vovrosh, P. Bouyer, G. Condon, E. Rasel, C. Schubert, W. P. Schleich, and A. Roura, Taking atom interferometric quantum sensors from the laboratory to real-world applications, Nat. Rev. Phys. **1**, 731 (2019).

[4] A. D. Cronin, J. Schmiedmayer, and D. E. Pritchard, Optics and interferometry with atoms and molecules, Rev. Mod. Phys. **81**, 1051 (2009).

[5] B. Barrett, R. Geiger, I. Dutta, M. Meunier, B. Canuel, A. Gauguet, P. Bouyer, and A. Landragin, The Sagnac effect: 20 years of development in matter-wave interferometry, C. R. Phys. **15**, 875 (2014).

[6] F. Riehle, T. Kisters, A. Witte, J. Helmcke, and C. J. Bordé, Optical Ramsey spectroscopy in a rotating frame: Sagnac effect in a matter-wave interferometer, Phys. Rev. Lett. **67**, 177 (1991).

[7] D. S. Durfee, Y. K. Shaham, and M. A. Kasevich, Long-term stability of an area-reversible atom-interferometer sagnac gyroscope, Phys. Rev. Lett. **97**, 240801 (2006).

[8] R. Dumke, T. Müther, M. Volk, W. Ertmer, and G. Birkl, Interferometer-type structures for guided atoms, Phys. Rev. Lett. **89**, 220402 (2002).

[9] Y. Japha, O. Arzouan, Y. Avishai, and R. Folman, Using time-reversal symmetry for sensitive incoherent matter-wave sagnac interferometry, Phys. Rev. Lett. **99**, 060402 (2007).

[10] T. Müller, X. Wu, A. Mohan, A. Eyvazov, Y. Wu, and R. Dumke, Towards a guided atom interferometer based on a superconducting atom chip, New J. Phys. **10**, 073006 (2008).

[11] H. Yan, Guided atom gyroscope on an atom chip with symmetrical state-dependent microwave potentials, Appl. Phys. Lett. **101**, 194102 (2012).

[12] C. Ryu and M. G. Boshier, Integrated coherent matter wave circuits, New J. Phys. **17**, 092002 (2015).

[13] P. Navez, S. Pandey, H. Mas, K. Poulios, T. Fernholz, and W. V. Klitzing, Matter-wave interferometers using TAAP rings, New J. Phys. **18**, 075014 (2016).

[14] C. L. G. Alzar, Compact chip-scale guided cold atom gyrometers for inertial navigation: Enabling technologies and design study, AVS Quantum Sci. **1**, 014702 (2019).

[15] S. Moukouri, Y. Japha, M. Keil, T. David, D. Groswasser, M. Givon, and R. Folman, Multi-pass guided atomic Sagnac interferometer for high-performance rotation sensing, arXiv:2107.03446.

[16] V. Vali and R. W. Shorthill, Fiber ring interferometer, Appl. Opt. **15**, 1099 (1976).

[17] W. M. Itano, J. C. Bergquist, J. J. Bollinger, J. M. Gilligan, D. J. Heinzen, F. L. Moore, M. G. Raizen, and D. J. Wineland, Quantum projection noise: Population fluctuations in two-level systems, Phys. Rev. A **47**, 3554 (1993).

[18] S. Templier, P. Cheiney, Q. d'Armagnac de Castanet, B. Gouraud, H. Porte, F. Napolitano, P. Bouyer, B. Battelier, and B. Barrett, Tracking the vector acceleration with a hybrid quantum accelerometer triad, Sci. Adv. **8**, eadd3854 (2022).

[19] F. A. Narducci, A. T. Black, and J. H. Burke, Advances toward fieldable atom interferometers, Adv. Phys.: X **7**, 1946426 (2022).

[20] F. Guattari, C. Moluçon, A. Bigueur, E. Ducloux, E. d. Toldi, J. Honthaas, and H. Lefèvre, Touching the limit of fog angular random walk: Challenges and applications, in *Proceedings of the 2016 DGON Intertial Sensors and Systems (ISS)* (IEEE, New York, 2016), pp. 1–13.

[21] Y. N. Korkishko, V. A. Fedorov, V. E. Prilutskiy, V. G. Ponomarev, I. V. Fedorov, S. M. Kostritskii, I. V. Morev, D. V. Obuhovich, S. V. Prilutskiy, A. I. Zuev, and V. K. Varnakov, High-precision inertial measurement unit IMU-5000, in *Proceedings of the 2018 IEEE International Symposium on Inertial Sensors and Systems (INERTIAL)* (IEEE, New York, 2018), pp. 1–4.

[22] S. Wu, Y.-J. Wang, Q. Diot, and M. Prentiss, Splitting matter waves using an optimized standing-wave light-pulse sequence, Phys. Rev. A **71**, 043602 (2005).

[23] Y.-J. Wang, D. Z. Anderson, V. M. Bright, E. A. Cornell, Q. Diot, T. Kishimoto, M. Prentiss, R. A. Saravanan, S. R. Segal, and S. Wu, Atom Michelson interferometer on a chip using a Bose-Einstein condensate, Phys. Rev. Lett. **94**, 090405 (2005).

[24] O. Garcia, B. Deissler, K. J. Hughes, J. M. Reeves, and C. A. Sackett, Bose-Einstein-condensate interferometer with macroscopic arm separation, Phys. Rev. A **74**, 031601(R) (2006).

[25] S. Wu, E. Su, and M. Prentiss, Demonstration of an area-enclosing guided-atom interferometer for rotation sensing, Phys. Rev. Lett. **99**, 173201 (2007).

[26] L. Qi, Z. Hu, T. Valenzuela, Y. Zhang, Y. Zhai, W. Quan, N. Waltham, and J. Fang, Magnetically guided cesium interferometer for inertial sensing, Appl. Phys. Lett. **110**, 153502 (2017).

[27] J. H. T. Burke and C. A. Sackett, Scalable Bose-Einstein-condensate Sagnac interferometer in a linear trap, Phys. Rev. A **80**, 061603(R) (2009).

[28] G. B. Jo, Y. Shin, S. Will, T. A. Pasquini, M. Saba, W. Ketterle, D. E. Pritchard, M. Vengalattore, and M. Prentiss, Long phase coherence time and number squeezing of two Bose-Einstein condensates on an atom chip, Phys. Rev. Lett. **98**, 030407 (2007).

[29] E. R. Moan, R. A. Horne, T. Arpornthip, Z. Luo, A. J. Fallon, S. J. Berl, and C. A. Sackett, Quantum rotation sensing with dual sagnac interferometers in an atom-optical waveguide, Phys. Rev. Lett. **124**, 120403 (2020).

[30] A. S. Arnold, C. MacCormick, and M. G. Boshier, Adaptive inelastic magnetic mirror for Bose-Einstein condensates, Phys. Rev. A **65**, 031601(R) (2002).

[31] H. Müller, S. W. Chiow, and S. Chu, Atom-wave diffraction between the Raman-Nath and the Bragg regime: Effective Rabi frequency, losses, and phase shifts, Phys. Rev. A **77**, 023609 (2008).

[32] E. Torrontegui, S. Ibáñez, X. Chen, A. Ruschhaupt, D. Guéry-Odelin, and J. G. Muga, Fast atomic transport without vibrational heating, Phys. Rev. A **83**, 013415 (2011).

[33] J. H. T. Burke, B. Deissler, K. J. Hughes, and C. A. Sackett, Confinement effects in a guided-wave atom interferometer with millimeter-scale arm separation, Phys. Rev. A **78**, 023619 (2008).

[34] M. Lewenstein and L. You, Quantum phase diffusion of a Bose-Einstein condensate, Phys. Rev. Lett. **77**, 3489 (1996).

[35] J. Javanainen and M. Wilkens, Phase and phase diffusion of a split Bose-Einstein condensate, Phys. Rev. Lett. **78**, 4675 (1997).

[36] A. J. Leggett and F. Sols, Comment on "Phase and phase diffusion of a split Bose-Einstein condensate", Phys. Rev. Lett. **81**, 1344 (1998).

[37] J. Javanainen and M. Wilkens, Javanainen and Wilkens reply, Phys. Rev. Lett. **81**, 1345 (1998).

[38] R. Bistritzer and E. Altman, Intrinsic dephasing in one-dimensional ultracold atom interferometers, Proc. Natl. Acad. Sci. USA **104**, 9955 (2007).

[39] A. A. Burkov, M. D. Lukin, and E. Demler, Decoherence dynamics in low-dimensional cold atom interferometers, Phys. Rev. Lett. **98**, 200404 (2007).

[40] S. Hofferberth, I. Lesanovsky, B. Fischer, T. Schumm, and J. Schmiedmayer, Non-equilibrium coherence dynamics in one-dimensional Bose gases, Nature (London) **449**, 324 (2007).

[41] E. O. Ilo-Okeke and A. A. Zozulya, Atomic population distribution in the output ports of cold-atom interferometers with optical splitting and recombination, Phys. Rev. A **82**, 053603 (2010).

[42] J. Grond, U. Hohenester, I. Mazets, and J. Schmiedmayer, Atom interferometry with trapped Bose–Einstein condensates: Impact of atom–atom interactions, New J. Phys. **12**, 065036 (2010).

[43] H. P. Stimming, N. J. Mauser, J. Schmiedmayer, and I. E. Mazets, Dephasing in coherently split quasicondensates, Phys. Rev. A **83**, 023618 (2011).

[44] A. Fallon, R. H. Leonard, and C. A. Sackett, Estimation of phase diffusion rates in a condensate interferometer using the Gross–Pitaevskii equation, J. Phys. B: At. Mol. Opt. Phys. **48**, 205301 (2015).

[45] R. Geiger, V. Ménoret, G. Stern, N. Zahzam, P. Cheinet, B. Battelier, A. Villing, F. Moron, M. Lours, Y. Bidel *et al.*, Detecting inertial effects with airborne matter-wave interferometry, Nat. Commun. **2**, 474 (2011).

[46] L. C. Ng and D. J. Pines, Characterization of ring laser gyro performance using the Allan variance method, J. Guid. Control. Dyn. **20**, 211 (1997).

[47] H. Kim, K. Krzyzanowska, K. C. Henderson, C. Ryu, E. Timmermans, and M. Boshier, One second interrogation time in a 200 round-trip waveguide atom interferometer, arXiv:2201.11888v3.

[48] M. C. Cassidy, M. G. Boshier, and L. E. Harrell, Improved optical standing-wave beam splitters for dilute Bose–Einstein condensates, J. Appl. Phys. **130**, 194402 (2021).

[49] Y. N. Korkishko, V. A. Fedorov, V. E. Prilutskiy, V. G. Ponomarev, I. V. Morev, D. V. Obuhovich, I. Fedorov, and N. Krobka, Investigation and identification of noise sources of high precision fiber optic gyroscopes, in *Proceedings of the 20th Saint Petersburg International Conference on Integrated Navigation Systems* (IEEE, New York, 2013), pp. 59–62.